

Diffusion imaging with stimulated echoes:
signal models and experiment design

Daniel C. Alexander¹

Tim B. Dyrby²

¹Centre for Medical Image Computing,
Department of Computer Science, University College London,
Gower Street, London WC1E 6BT, UK.

²Danish Research Centre for Magnetic Resonance, Copenhagen
University Hospital Hvidovre, Hvidovre, Denmark.

4964 words in main text excluding abstract, appendix, acknowledgement,
displayed equations, and captions. 195 in abstract. 463 in appendix. 7560
in latex file.

Correspondence: D.Alexander@cs.ucl.ac.uk.

Abstract

Purpose: Stimulated echo acquisition mode (STEAM) diffusion MRI can be advantageous over pulsed-gradient spin-echo (PGSE) for diffusion times that are long compared to T_2 . It is important therefore for biomedical diffusion imaging applications at 7T and above where T_2 is short. However, imaging gradients in the STEAM sequence contribute much greater diffusion weighting than in PGSE, but are often ignored during post-processing. We demonstrate here that this can severely bias parameter estimates.

Method: We present models for the STEAM signal for free and restricted diffusion that account for crusher and slice-select (butterfly) gradients to avoid such bias. The butterfly gradients also disrupt experiment design, typically by skewing gradient-vectors towards the slice direction. We propose a simple compensation to the diffusion gradient vector specified to the scanner that counterbalances the butterfly gradients to preserve the intended experiment design.

Results: High-field data fixed monkey brain experiments demonstrate the need for both the compensation during acquisition and correct modelling during post-processing for both diffusion tensor imaging and ActiveAx axon-diameter index mapping. Simulations support the results and indicate a similar need in in-vivo human applications.

Conclusion: Correct modelling and compensation are important for practical applications of STEAM diffusion MRI.

Keywords: Diffusion MRI; diffusion tensor imaging; HARDI; STEAM; stimulated echo; ActiveAx; axon diameter; brain; microstructure

1 Introduction

Stimulated echo acquisition mode (STEAM) diffusion MRI [1, 2] offers advantages over the more common pulsed-gradient spin-echo (PGSE) diffusion MRI when T_2 is short compared to the diffusion time and $T_1 > T_2$. Whereas T_2 -decay occurs throughout the PGSE sequence, in STEAM the signal decays instead with rate T_1 during the mixing time τ_m , which determines the diffusion time. Thus, despite a factor of two reduction in signal from loss of one coherence pathway, STEAM retains more signal than PGSE for large enough diffusion time.

STEAM diffusion MRI is common in tissue with short T_2 , such as muscle or cartilage, e.g. [3]. Current in-vivo human-brain diffusion MRI applications usually do not benefit from STEAM, because T_2 at 1.5T or 3T is relatively long compared to typical diffusion times. However, T_2 decreases and T_1 increases as field strength increases. Early evidence [4] already suggests benefits of STEAM for in-vivo human-brain diffusion tensor imaging (DTI) at 7T. Ex-vivo q -space studies of brain tissue, e.g. [5, 6, 7], usually prefer STEAM over PGSE, because they use high field preclinical scanners, tissue fixation further reduces T_2 , and lower sample temperature reduces diffusivity increasing necessary diffusion times [8, 9]. Translation of advanced diffusion MRI techniques to high field in-vivo human applications is likely to rely on STEAM in place of PGSE. For example, diffusion spectrum imaging [10] requires high b -values and consequently long echo time in PGSE, which becomes infeasible as T_2 decreases. Also, microstructure imaging techniques, such as ActiveAx [11] and AxCaliber [6], require long diffusion times to ensure sensitivity to large diameter axons [12].

Imaging gradients in diffusion MRI add diffusion weighting and “cross-terms” in the b -matrix [13]. The most significant contributions are usually from the crusher and slice-select gradients, so-called “butterfly gradients”. In PGSE, their contribution to the diffusion weighting is usually negligible in practice, because the diffusion time for the butterfly gradients is only a few milliseconds (the length of the refocussing pulse). However, in STEAM, that contribution is typically much more significant, because the diffusion time is approximately τ_m . Nevertheless, previous work with STEAM diffusion MRI, such as [6, 7], follows standard practice for PGSE and ignores the effect.

In this paper, we derive models for the STEAM signal that account for the diffusion weighting of the butterfly gradients and avoid unnecessary bias in parameter estimation during post-processing. Specifically, we adapt the DTI b -matrix calculations in [13] for STEAM and we derive new models for restricted diffusion using the Gaussian Phase Distribution (GPD) approximation. The latter extend standard PGSE models for restricted diffusion in spheres [14], cylinders [15], and more general restricting geometries [16] for use with STEAM. In addition, we propose a simple compensation of the diffusion gradient vector during acquisition that counterbalances the diffusion weighting of the butterfly gradients. This avoids disruptions to the experiment design (the intended set of b -values, gradient directions, etc), which arise from the butterfly gradients skewing the effective diffusion weighting towards towards the slice direction.

Simulation and fixed-brain experiments use DTI and ActiveAx, orientationally invariant axon density and diameter index mapping, to demonstrate that ignoring the butterfly gradients in STEAM post processing biases parameter estimates. Using the new models avoids unnecessary bias. Moreover, these

high angular resolution diffusion imaging (HARDI) applications demonstrate how the compensation corrects significant disruption to the experiment design leading to further improvements in accuracy and precision of parameter estimates. In combination, the new models and the compensation provide the essential tools for using STEAM in a wide range of practical applications.

2 Methods

This section introduces the STEAM diffusion-weighted pulse sequence. It then outlines various candidate signal models for both free, the diffusion tensor (DT) model, and restricted diffusion that support parameter estimation from measured data. The last subsection specifies the compensation for preserving experiment design.

2.1 STEAM pulse sequence

The signal models in subsequent sections assume the idealized STEAM pulse sequence in figure 1, which consists of:

1. An initial 90° pulse to align the spins.
2. A diffusion gradient pulse with duration δ_d and constant gradient vector \mathbf{G}_d , which starts at time zero.
3. A gap of length τ_1 with no gradients.
4. A crusher pulse, which starts at time $\delta_d + \tau_1$ and lasts for time δ_c with constant gradient vector \mathbf{G}_c .

5. A slice-select pulse, which starts immediately after the crusher pulse at time $\delta_d + \tau_1 + \delta_c$. The slice-select pulse lasts for $2\delta_s$ with constant gradient vector \mathbf{G}_s . However, the second 90° pulse occurs at the centre of the slice-select pulse, so only the first half contributes diffusion weighting. Thus, to calculate the diffusion weighted signal, we consider the slice-select pulse to have length δ_s , starting at $\delta_d + \tau_1 + \delta_c$.
6. A mixing time τ_m , which starts after the second 90° pulse.
7. A spoiler pulse during the mixing time, which contributes no diffusion weighting so we do not consider it further. Additional crusher pulses also occur during τ_m that do not contribute diffusion weighting. Non-contributing pulses are dashed in figure 1.
8. A third 90° pulse, which occurs at the end of the mixing time at the centre of a second slice-select pulse. The diffusion weighting part of the second slice-select is equal to the first, starting at time $\delta_d + \tau_1 + \delta_c + \delta_s + \tau_m$.
9. A second crusher gradient equal to the first at time $\delta_d + \tau_1 + \delta_c + 2\delta_s + \tau_m$.
10. A gap of length τ_2 with no gradients.
11. A second diffusion gradient pulse equal to the first at time $\delta_d + \tau_1 + \tau_2 + 2\delta_c + 2\delta_s + \tau_m$.

2.2 Signal models

We consider three approximations to the signal that account for the butterfly gradients in different ways:

- Approximation 1 (A1) ignores the butterfly gradients and considers only the diffusion gradients.
- Approximation 2 (A2) identifies an effective diffusion gradient \mathbf{G}_d' that incorporates the diffusion weighting of the diffusion and butterfly gradients. A simple choice is

$$\mathbf{G}_d' = \mathbf{G}_d + \delta_c \tau_{dc} (\delta_d \tau_{dd})^{-1} \mathbf{G}_c + \delta_s \tau_{ds} (\delta_d \tau_{dd})^{-1} \mathbf{G}_s, \quad (1)$$

where τ_{dc} , τ_{dd} , and τ_{ds} are functions of the pulse timings defined in the Appendix, Eq. 11. Section A.2 in the Appendix derives Eq. 1 and discusses other possible choices for \mathbf{G}_d' .

- Approximation 3 (A3) uses the Gaussian phase distribution (GPD) approximation to derive models that account explicitly for the butterfly gradients.

2.2.1 Diffusion tensor imaging

A1 uses the simplest model for DTI, where the signal

$$S = S_0 \exp\left(-b \hat{\mathbf{G}}_d D \hat{\mathbf{G}}_d\right), \quad (2)$$

$$b = (\Delta - \delta_d/3)(\gamma \delta_d |\mathbf{G}_d|)^2, \quad (3)$$

$$\Delta = \tau_m + \delta_d + 2\delta_s + 2\delta_c + \tau_1 + \tau_2, \quad (4)$$

D is the DT, γ is the gyromagnetic ratio, $\hat{\mathbf{G}}_d$ is a unit vector in the direction of \mathbf{G}_d , and S_0 is the signal with $b = 0$.

A2 also uses Eq. 2, but with \mathbf{G}_d' from Eq. 1 replacing \mathbf{G}_d .

A3 uses the full b -matrix, analogous to [13] for PGSE, rather than the single b -value in A1 and A2. The Appendix, section A.1, gives the formula.

By assuming a single b -value, A1 and A2 ignore the cross terms in the b -matrix, which express the interaction between gradient components with different orientation [13]. A1 is exact only when $\mathbf{G}_c = \mathbf{G}_s = 0$. A2 is exact only when \mathbf{G}_d , \mathbf{G}_c and \mathbf{G}_s all have the same orientation. A3 accounts for all cross terms so is always exact for Gaussian dispersion assumed in DTI.

2.2.2 Restricted diffusion

The GPD approximation to the signal from particles exhibiting restricted diffusion is [16]

$$S = S_0 \exp \left(-\frac{\gamma^2}{d^2} \sum_{k=0}^{\infty} \frac{B_k I_k}{\lambda_k^2} \right), \quad (5)$$

where d is the free diffusivity within the restricting domain, B_k and λ_k are constants that depend on only the geometry of the domain, and I_k depends also on the pulse sequence. For domains with simple geometric shapes such as spheres, separated planes, and cylinders, B_k and λ_k have simple analytic form [16]. For PGSE,

$$I_k = G_d^2 (2\delta_d \lambda_k^2 d - 2 + 2Y_k(-\delta_d) + 2Y_k(-\Delta) - Y_k(\delta_d - \Delta) - Y_k(-\delta_d - \Delta)), \quad (6)$$

where G_d is the component of \mathbf{G}_d in the restricted direction, and $Y_k(x) = \exp(\lambda_k^2 dx)$.

Eq. 6 assumes perfectly rectangular diffusion pulses and ignores any diffusion weighting from other pulses. Thus A1 uses Eq. 6 adapted for STEAM by setting Δ as in Eq. 4.

A2 uses the same formula as A1 with \mathbf{G}_d' from Eq. 1 replacing \mathbf{G}_d .

A3 redefines I_k to accommodate the additional pulses. Section A.3 in the appendix provides the formula.

For restricted diffusion, A1, A2 and A3 are all approximations, since they rely on the GPD approximation. However, A3 accounts for cross terms between the separate pulses, which A1 and A2 ignore.

2.3 Compensation

To achieve a particular experiment design, we can compensate for the diffusion weighting of the butterfly gradients using the inverse of approximation A2: for intended gradient vector \mathbf{G} , we acquire instead \mathbf{G}_d that produces \mathbf{G}_d' close to \mathbf{G} . For example, directly from Eq. 1, set

$$\mathbf{G}_d = \mathbf{G} - \delta_c \tau_{dc} (\delta_d \tau_{dd})^{-1} \mathbf{G}_c - \delta_s \tau_{ds} (\delta_d \tau_{dd})^{-1} \mathbf{G}_s. \quad (7)$$

The weightings $\delta_c \tau_{dc} (\delta_d \tau_{dd})^{-1}$ and $\delta_s \tau_{ds} (\delta_d \tau_{dd})^{-1}$ depend only on the timings of the pulses so are constant within one HARDI shell, but may vary between shells or measurements with different b -value or diffusion time.

3 Results

The central hypothesis is that the new models, A2 or A3, and/or compensation are necessary, because the standard treatment of STEAM diffusion MRI, A1 without compensation, lacks sufficient accuracy. This section compares signal models A1, A2 and A3, and evaluates the impact of compensation within the context of adapting ActiveAx [11] for STEAM. However,

we reserve a detailed comparison of STEAM versus PGSE for DTI and/or ActiveAx for future work.

3.1 ActiveAx protocols

The experiments use three imaging protocols. ActiveAxPGSE is the PGSE ActiveAx imaging protocol from [12] with maximum gradient strength $G_{\max} = 300 \text{ mTm}^{-1}$. ActiveAxSTEAM is a STEAM protocol, also with $G_{\max} = 300 \text{ mTm}^{-1}$, optimised for ActiveAx by adapting the experiment design optimization in [12, 17] for STEAM. The adaptation simply replaces the estimate of the signal to noise ratio, which is proportional to $\exp(-\tau_e/T_2)$ for PGSE and $\exp(-\tau_e/T_2) \exp(-\tau_m/T_1)$ for STEAM. Table 1 shows the settings for each of the three HARDI shells that constitute each protocol. The third protocol, ActiveAxSTEAMCOMP, adapts each \mathbf{G}_d in ActiveAxSTEAM according to the compensation in section 2.3.

Every image in ActiveAxSTEAM and ActiveAxSTEAMCOMP has $\delta_c = 1.5 \text{ ms}$, $\mathbf{G}_c = (0, 0, 0.15) \text{ Tm}^{-1}$, $\delta_s = 1.0 \text{ ms}$, $\mathbf{G}_s = (0, 0, 0.14) \text{ Tm}^{-1}$, and $\tau_2 = 0$. As an indication of the butterfly gradients' impact, the b -value from the crushers alone is 250 s mm^{-2} for the $b = 3425 \text{ s mm}^2$ shell of ActiveAxSTEAM, in contrast to 10 s mm^{-2} for ActiveAxPGSE. Since \mathbf{G}_c and \mathbf{G}_s are both along the slice direction $(0, 0, 1)$, the compensation $\mathbf{G} - \mathbf{G}_d$, from Eq. 7, is along the negative slice direction; $|\mathbf{G} - \mathbf{G}_d| = 43.4 \text{ mTm}^{-1}$, 68.5 mTm^{-1} and 76.0 mTm^{-1} , for the three shells respectively. To illustrate practical implementation of ActiveAxSTEAMCOMP, the first gradient direction in the $b = 3425 \text{ s mm}^2$ shell is $\{0.85, 0.48, 0.23\}$ and $|\mathbf{G}_d| = 113.5 \text{ mTm}^{-1}$, so the intended gradient vector is $\{95.9, 54.4, 26.6\} \text{ mTm}^{-1}$.

Eq. 7, tells us to type $\mathbf{G}_d = \{95.9, 54.4, -41.9\} \text{ mT m}^{-1}$ ($\hat{\mathbf{G}}_d = \{0.81, 0.46, -0.35\}$ and $|\mathbf{G}_d| = 118 \text{ mT m}^{-1}$) into the scanner console instead.

Figure 2 shows the distribution of effective gradient directions, i.e. the orientation of \mathbf{G}_d' from Eq. 1, for the $b = 3425 \text{ s mm}^{-2}$ shell of ActiveAxSTEAM and ActiveAxSTEAMCOMP to illustrate the disruption to the HARDI design. Without compensation, the butterfly gradients skew the effective gradient directions strongly towards the slice direction. The compensated protocol has evenly distributed effective gradient directions.

3.2 Data acquisition

We acquire data from a fixed monkey brain, prepared as in [8], using all three protocols in a single contiguous session. The live monkey was handled and cared for on the Island of St. Kitts according to a protocol approved by the local ethics committee (The Caribbean Primate Center of St. Kitts). The image volume is 256×128 voxels in plane with 15 contiguous sagittal slices including the mid-sagittal plane; voxels are 0.5mm isotropic.

The ActiveAxSTEAMCOMP acquisition has two imperfections. First, the butterfly gradients affect the nominal $b = 0$ images, as well as the diffusion weighted images. In theory, the compensation works for them too by adding non-zero \mathbf{G}_d in the negative slice direction. However, imperfect r.f. pulses prevent use of the compensation for the nominal $b = 0$ images in practice. In the absence of a strong diffusion gradient, the compensation counteracts the effect of the crusher gradients, allowing additional echoes to affect the signal and leading to severe image artifacts. Thus the nominal $b = 0$ images remain uncompensated with $\mathbf{G}_d = \mathbf{0}$.

The second imperfection occurs in a small number of measurements for which the slice-direction components of \mathbf{G}_d after compensation exceed G_{\max} . The scanner automatically truncates that component at G_{\max} , so the effective gradient vector departs from what the compensated protocol intends. The second imperfection is avoidable by negating the original gradient direction before compensation. However, we retain the imperfection here, as it (a) affects only two measurements significantly (both in the $b = 2306 \text{ s mm}^{-2}$ shell; see figure 4 later) and (b) helps to illustrate differences between A1 and A2 (figure 4).

3.3 DTI

This section evaluates bias in the DT estimated using A1, A2 and A3 from both compensated and uncompensated acquisition. Simulation experiments quantify the effects in idealised conditions. Experiments with the monkey brain data confirm the trends on measured data. Both experiments focus on the $b = 3425 \text{ s mm}^{-2}$ shell from the ActiveAxSTEAM protocol, which has b -value typical for ex-vivo DTI [8] and long τ_m that exploits the benefits of STEAM, but also emphasises the diffusion weighting of the butterfly gradients.

3.3.1 Simulations

Experiment. The synthetic data do not reflect the two imperfections in the scanner data, so the nominal $b = 0$ measurements are compensated, and no truncation of the gradient vectors at G_{\max} occurs (no measurements in the $b = 3425 \text{ s mm}^{-2}$ shell are affected by this anyway). Eqs. 8 and 10 in the

Appendix provides synthetic data from the DT model.

The experiments use two DTs, one with eigenvalues $\{0.6, 0.2, 0.2\} \times 10^{-9} \text{ m}^2\text{s}^{-1}$, which are typical of coherent white matter in fixed brain tissue at this b value, and the other $\{0.4, 0.4, 0.4\} \times 10^{-9} \text{ m}^2\text{s}^{-1}$, which is isotropic with the same trace. The anisotropic DT has two variations: the first has principal eigenvector $\mathbf{e}_1 = \{0, 0, 1\}$, so that \mathbf{G}_c and \mathbf{G}_s are parallel to the fibre direction, and the second has $\mathbf{e}_1 = \{1, 0, 0\}$, so they are perpendicular.

Each experiment adds Rician noise so that the signal to noise ratio of the unweighted signal is 20. Weighted linear least squares fitting [18] estimates the DT using each approximation from which we compute the eigenvalues, fractional anisotropy (FA) and \mathbf{e}_1 . We repeat the procedure over 10000 independent noise trials and compute the mean and standard deviation of the largest eigenvalue λ_1 and the FA. We also compute the mean angle α between the estimated and true \mathbf{e}_1 , for the anisotropic DTs. For all DTs, we compute the direction concentration $\gamma = -\log(1 - E)$, where E is the largest eigenvalue of the mean dyadic tensor [19]. The direction concentration is zero for an isotropic set of directions and increases as the variance of the distribution decreases, reaching infinity when all align perfectly. Typical values of γ for similar noise trials with anisotropic tensors in [19] are 6 to 8. Unbiased noise trials with the isotropic tensor should produce γ close to zero.

To give some idea of the significance of the effects in a human imaging protocol, we repeat the experiment using in-vivo settings for a 3T clinical scanner. The protocol has 7 nominal $b = 0$ images and 60 gradient directions with $b = 1007 \text{ s mm}^{-2}$; $|\mathbf{G}_d| = 40 \text{ mT m}^{-1}$, $\tau_m = 120 \text{ ms}$, $\delta_d = 8 \text{ ms}$, $\tau_1 = \tau_2 = 0$, $\delta_c = 0.5 \text{ ms}$, $\delta_s = 5.5 \text{ ms}$, $\mathbf{G}_c = \{20, 20, 20\} \text{ mT m}^{-1}$ and $\mathbf{G}_s = \{0, 0, 6\} \text{ mT m}^{-1}$. The butterfly gradients are weaker than the ex-vivo

protocol, because the voxel size is larger (2.3 mm isotropic). The test DTs have eigenvalues $\{1.7, 0.2, 0.2\} \times 10^{-9} \text{ m}^2 \text{ s}^{-1}$ and $\{0.7, 0.7, 0.7\} \times 10^{-9} \text{ m}^2 \text{ s}^{-1}$.

Results. Tables 2 and 3 list statistics for the fixed-tissue simulations with the anisotropic and isotropic DTs, respectively. Note that perfect compensation makes A1 and A2 equivalent.

Without compensation, A1 shows significant bias in FA, λ_1 and \mathbf{e}_1 with both orientations of the anisotropic DT. Bias is most severe for \mathbf{e}_1 parallel to the butterfly gradients where the DT estimation completely fails. Estimates of the isotropic DT show artifactual non-zero FA and significant direction concentration: $\gamma = 1.5$ means 95% of directions are within 6° of the mean. Compensation dramatically improves A1. Some downward bias remains in both FA and λ_1 of the anisotropic DTs, but the bias is similar for both orientations. Compensation largely removes artifactual non-zero FA and orientational bias in the isotropic DT estimates: $\gamma = 0.4$ is typical for a uniformly distributed random sample of 10000 directions and the 95%-angle is over 25° .

Without compensation, A2 and A3 produce very similar results. Both significantly reduce bias compared to A1, although bias remains orientationally dependent and is strongest with parallel \mathbf{G}_c and \mathbf{G}_s . Compensation reduces bias and variance of parameter estimates from A3, especially for parallel \mathbf{e}_1 , and removes orientational dependence. With compensation, A3 shows no benefit over A1 or A2.

Tables 4 and 5 show corresponding results from the in-vivo human protocol. Without compensation, A1 still produces considerable bias, which A2 or A3 reduces. The compensation provides only minor further improvements with

A3.

Conclusions. Two separate effects cause unnecessary bias in the parameter estimates: model inaccuracy and disrupted experiment design. Model inaccuracy is the dominant cause of the large bias from A1 without compensation. The large reduction in bias from replacing A1 with A2 or A3 demonstrates the importance of accounting for the butterfly gradients in the model. The lack of performance difference between A2 and A3 shows that the cross terms in the b -matrix are negligible.

The bias we observe in FA and λ_1 from A3 with compensation is unavoidable, since the model is exact and the experiment design is not disrupted. It comes from Jones’ “squashed-peanut” effect [18]: a Rician noise effect as measurements with gradient parallel to \mathbf{e}_1 approach the noise floor. Differences in results from A3 with and without compensation show the effect of the experiment design disruption. The disruption to the experiment design affects parameter estimates most strongly with parallel butterfly gradients, because the additional diffusion weighting in the fibre direction pushes parallel signals further into the noise floor. Compensation reduces bias and improves precision by removing the experiment design disruption, which also removes the orientational dependence of the bias and variance.

The performance differences are less marked in the human protocol, because the butterfly gradients are smaller. However, values of α between 2.5° and 12° that we observe for A1 without compensation are at least as large as orientational bias incurred by failing to account for small head motions in the b -matrix, which [20] finds sufficient to disrupt tractography.

3.3.2 Monkey data

Experiment. We fit the DT to the $b = 3425\text{s mm}^{-2}$ shell of ActiveAxSTEAM and ActiveAxSTEAMCOMP, as well as the $b = 3084\text{s mm}^{-2}$ shell of ActiveAxPGSE, using weighted linear least squares and construct colour-coded \mathbf{e}_1 maps [21]. We quantify the orientational similarity between pairs of DT volumes by computing the mean over the brain of the absolute dot product of principal directions weighted by DT linearity [22].

Results. Figure 3 compares maps from PGSE with STEAM for each approximation qualitatively. The number next to each STEAM map is the orientational similarity with PGSE; higher numbers show greater agreement. The number next to the PGSE map is the orientational similarity of the $b = 2243\text{s mm}^{-2}$ and $b = 3084\text{second mm}^{-2}$ shells of ActiveAxPGSE.

For ActiveAxSTEAM, A1 introduces upward bias in FA in the superior half of the brain where diffusion should be close to isotropic, such as the area in the cyan box on the PGSE map. The maps also show orientation bias towards the left-right slice direction (the map appears red). The white boxes show bias in anisotropic regions: the left box shows severely biased orientation estimates (some voxels appear green rather than red) in the corpus callosum, where the fibres are parallel to the butterfly gradients; the right box shows less biased orientation estimates in the fornix, which has perpendicular fibres. A2 and A3 are qualitatively indistinguishable from one another and are more consistent with the PGSE map than A1, e.g. in the white boxes. However, they still show upward bias in FA together with consistent artifactual orientation in isotropic regions (blue/green colour in cyan box region).

For ActiveAxSTEAMCOMP, all maps appear more similar to PGSE than the uncompensated maps and have low FA in the cyan box region. A2 and A3 are indistinguishable. The compensated A1 map shows generally higher anisotropy, for example in the cerebellum marked by the yellow box. Some differences in orientation between the compensated STEAM and PGSE maps still appear, for example in the area marked by the green box.

Conclusions. Differences among the maps broadly reflect the bias we observe in the simulation experiment. A1 uncompensated shows artifactual raised FA in isotropic regions and orientation bias towards left-right arises from the butterfly gradients enhancing attenuation in that direction. Moreover, the white boxes demonstrate the orientational dependence of the bias: as in the simulations it is most significant when \mathbf{e}_1 and butterfly gradients are parallel.

Compensation generally reduces bias. Differences between A1 and A2 with compensation appear because A1 does not account for the imperfections in the compensation. Maps from ActiveAxSTEAMCOMP with A3 and PGSE do not match perfectly, because the diffusion times and b -values differ.

The trends in quantitative orientational similarity confirm the intuition from the qualitative maps.

3.4 Restricted diffusion

This section uses the full ActiveAx data sets to demonstrate the models and compensation in an application that exploits restricted diffusion.

3.4.1 Simulations

The simulation experiment compares the accuracy of A1, A2 and A3 for restricted diffusion in a cylinder.

Experiment. The Monte-Carlo (MC) diffusion simulation system from [23], implemented in the Camino toolkit [24], provides synthetic ground truth measurements accounting precisely for all gradient pulses and timings. The simulations use ActiveAxSTEAM and ActiveAxSTEAMCOMP (from table 1) and this time include the imperfections in the ActiveAxSTEAMCOMP scanner data. Each simulation uses 160000 walkers and 5000 timesteps, which produces unbiased synthetic measurements with standard deviation less than $10^{-4}S_0$ [23]. All the walkers are trapped inside an impermeable cylinder (no extra-axonal contribution) with diameter $10\ \mu\text{m}$ and axis aligned with the slice direction; free diffusivity is $600\ \mu\text{m}^2\text{s}^{-1}$.

Results. Figure 4 compares the synthetic data from the MC simulation with predictions from A1, A2 and A3 for ActiveAxSTEAM (top row) and ActiveAxSTEAMCOMP (bottom row).

Without compensation, A1 shows large departures from the ground truth MC signals. A2 and A3 match the MC data much more closely: the maximum error against corresponding MC data points is 0.6 for A1, 0.04 for A2, and 0.01 for A3.

With compensation, large departures in A1 remain only in measurements with truncated gradient vectors (the two $b = 2306\ \text{s mm}^{-2}$ measurements with the most negative z -component in the left ellipse) and the uncompensated nominal $b = 0$ measurements (right ellipse). A2 is equivalent to A1 apart

from the imperfectly compensated measurements, which A2 predicts closely. A3 matches the MC data slightly better than A2, in particular for the $b = 2306 \text{ s mm}^{-2}$ shell (blue). A3 shows small departures from the MC data, especially in the high b -value shell (red).

Conclusions. A1 uncompensated predicts the signal poorly. In particular, ignoring the butterfly gradients predicts the highest signal to occur when \mathbf{G}_d is along the cylinder axis, whereas the peak actually occurs when \mathbf{G}_d' is perpendicular ($\cos \theta = 0$ in the figure).

In contrast to the free diffusion experiments, A3 does not provide exact predictions. Departures from the ground truth arise from violation of the GPD assumption. The departures reduce as cylinder diameter decreases. However, A3 does provide a benefit over A2 showing that cross terms are influential for restricted diffusion. The benefit also reduces as diameter decreases.

3.4.2 Monkey data

Experiment. We fit the minimal model of white matter diffusion (MMWMD) [11, 12] to the full data acquisition from each protocol in table 1 using the procedure outlined in [11]. The mixing time varies among the different shells in the STEAM protocols, so we first estimate T_1 from the nominal $b = 0$ images and fix its value for the subsequent MMWMD fitting.

Results. Figure 5 shows the axon diameter index maps from ActiveAxPGSE, and ActiveAxSTEAM and ActiveAxSTEAMCOMP with each approximation. The axon diameter index map from ActiveAxPGSE shows the familiar high-low-high trend from splenium through mid-body to genu, as in previous applications of ActiveAx [11, 12].

The maps from A1 show no clear trend for either ActiveAxSTEAM or ActiveAxSTEAMCOMP. However, all maps from A2 and A3 show the high-low-high trend, although the axon diameter index itself is consistently lower from STEAM than PGSE. A3 provides a greater range of axon diameter index and reproduces the trend more clearly than A2. Fitting errors (not shown) are significantly larger for A1 than either A2 or A3 and slightly lower for A3 than A2.

Conclusions. Severe model inaccuracy in A1 prevents sensible estimates of the axon diameter index; with ActiveAxSTEAMCOMP the imperfectly compensated measurements disrupt MMWMD fitting. A2 captures the imperfectly compensated measurements allowing the usual trend to emerge. Visible differences from A2 to A3 reflect lesser accuracy in A2, which the simulations demonstrate. Although we cannot verify directly that compensation and A3 produce better results, differences appearing among maps in figure 5 suggests that both are necessary.

Lower axon diameter index from STEAM compared to PGSE is somewhat counterintuitive, because longer diffusion times in STEAM increase sensitivity to larger axons over PGSE [12]. Thus we might expect the axon diameter index to increase. However, if no large axons are present, the STEAM data provide better information to reject any likelihood of their existence. This reduces the tails of the posterior distribution in the large diameter range that the PGSE data may permit, reducing the axon diameter index, which is the mean of the posterior [11]. Indeed, the axon diameter indices from A3 compensated are closer to the values we might expect [11] based on histology [25] than those from PGSE. However, that histology is from the brain of a different species, so further work is required to confirm this hypothesis.

4 Discussion

This paper highlights the need to account for the diffusion weighting of butterfly gradients in STEAM diffusion MRI. We provide signal models for both free and restricted diffusion that accommodate their effect. We also introduce a simple compensation to the acquired diffusion gradient that minimizes disruption to the experiment design the butterfly gradients cause. DTI and ActiveAx experiments with both synthetic and fixed monkey-brain data illustrate the potential for severe bias from ignoring the butterfly gradients (A1 uncompensated, the usual approach) and the major benefits of our improved models in avoiding unnecessary bias. They show further that retaining experiment design, in particular in HARDI applications, through our compensation further improves accuracy and precision of parameter estimates and avoids orientational dependence of both.

4.1 Recommendations

For acquisition, we recommend the compensation wherever possible in STEAM diffusion MRI, as it has no cost in terms of acquisition or post-processing. The compensation is straightforward to implement: it requires no pulse programming, simply adjustments to the scheme file specifying the gradient strengths and directions to the scanner. However, users should check how the scanner truncates or normalises gradient vectors to avoid the imperfections we mention in section 3.2. The compensation is particularly important in HARDI methods, but single-direction model-based STEAM diffusion MRI applications, such as [6, 7], are also likely to benefit significantly.

For data analysis, we strongly recommend avoiding A1, whereas A2 is sufficient for many practical circumstances, such as DTI. Although, A1 and A2 are equivalent in theory if the acquisition uses compensation, imperfect r.f. pulses sometimes prevent the compensation of low b -value measurements in practice, making A2 necessary. For models involving restricted diffusion, the slightly more accurate A3, which has a cost of about double the computation time, appears beneficial over A2.

4.2 Limitations and alternatives

The GPD approximation for restricted diffusion generally provides a reasonable approximation for the range of b -values and cylinder diameters relevant to the applications of interest here [26, 27]. However, it breaks down in some signal regimes; for example, it does not capture the characteristic q -space diffraction patterns in the restricted diffusion signal [28]. These circumstances require more precise estimates of the signal for example from Callaghan’s matrix formulation [29] and related numerical techniques that extend the idea to three-dimensions [30, 31].

The idealized pulse sequence model we use assumes zero ramp time for all pulses. The GPD method extends easily to accommodate non-zero ramp times [27], although in most practical situations they have little effect on the signal estimate.

The butterfly gradients in our preclinical ex-vivo application are stronger than in most in-vivo human applications, because the image slices are thinner. The strong gradients emphasize the disruption of the intended experiment design; the effect is less marked in in-vivo human applications, as tables 4

and 5 show. However, even small biases can disrupt subsequent analysis, such as tractography [20], so the methods we propose are still necessary.

We do not consider additional diffusion weighting from other imaging gradients, such as echo-planar imaging (EPI) gradient trains, which [13] demonstrate can be significant. Our data acquisition does not use EPI, so such contributions are irrelevant here. However, the general modelling and compensation approach extends naturally to account for these gradients if necessary. We also do not consider background gradients, which [32, 33] design versions of the STEAM pulse sequence to compensate for. Our compensation and models adapt naturally for those sequences and future work will study the necessity for such adaptations in brain-imaging applications.

The one-sidedness of the set of gradient directions affects the amount of bias that the butterfly gradients introduce to fitted parameters. Figure 2(a) shows that most of the directions in our protocols have positive z-component, so the butterfly gradients skew them away from the slice plane. Conversely, they skew most directions with negative z-component towards the slice plane. An even distribution of *signed* directions could reduce bias in parameter estimates, because the errors for positive and negative directions cancel to some extent. However, we do not recommend this solution, as it produces large fitting errors and is likely to mask undesirable effects on estimated parameters.

Other strategies for avoiding the effects of the butterfly gradients include simply turning the crushers off in the diffusion weighted measurements and relying on the diffusion gradients to crush unwanted echoes [4]. This requires sufficiently high diffusion weighting and is generally not possible for the nominal $b = 0$ images that most protocols require for normalization; the models

we propose are essential for explaining the signal in those images. Moreover, the slice-select gradients are always necessary in imaging applications.

4.3 Conclusions

We demonstrate here that imaging gradients in the STEAM sequence can severely disrupt HARDI experiment design and cause bias in parameter estimates if ignored. The models and methods we present solve these problems and enable widespread uptake of STEAM diffusion MRI. They allow future work to evaluate and exploit the potential benefits of STEAM especially for diffusion MRI on high field scanners where low T_2 prevents long diffusion time PGSE. In particular, they enable us to evaluate STEAM ActiveAx for better sensitivity to large axons, which is the focus of our current work.

Acknowledgements

We thank Prof Maurice Ptito (University of Montreal and Copenhagen University) and Mark Burke (Howard University) for providing the fixed monkey brain. Both authors acknowledge the support of European Commission Framework 7 through the CONNECT consortium. The EPSRC support DCA's work on this topic with grants EP/H046410/01 and EP/E007748. TBD was also supported by the Lundbeck foundation.

A Appendix

A.1 Gaussian dispersion and DTI

On the assumption of zero-mean Gaussian particle dispersion (the DT model), the general formula [34]

$$S = S_0 \exp(-B \cdot D), \quad (8)$$

predicts the signal, where $B = \gamma^2 \int \mathbf{F}(t)\mathbf{F}^T(t)dt$ is the b -matrix [13],

$$\mathbf{F}(t) = \int_0^t \mathbf{G}(t)dt, \quad (9)$$

$\mathbf{G}(t)$ is the gradient vector at time t , and \cdot is the matrix scalar product.

For idealised PGSE or STEAM with $\mathbf{G}_c = \mathbf{G}_s = 0$, i.e. approximations A1 or A2, Eq. 8 reduces to Eq. 2. However, for the full pulse sequence outlined in section 2.1, i.e. approximation A3,

$$\begin{aligned} B = & \delta_d^2 \tau_{dd} \mathbf{G}_d \mathbf{G}_d^T + \delta_c^2 \tau_{cc} \mathbf{G}_c \mathbf{G}_c^T + \delta_s^2 \tau_{ss} \mathbf{G}_s \mathbf{G}_s^T \\ & + \delta_d \delta_c \tau_{dc} (\mathbf{G}_d \mathbf{G}_c^T + \mathbf{G}_c \mathbf{G}_d^T) + \delta_d \delta_s \tau_{ds} (\mathbf{G}_d \mathbf{G}_s^T + \mathbf{G}_s \mathbf{G}_d^T) \\ & + \delta_c \delta_s \tau_{cs} (\mathbf{G}_c \mathbf{G}_s^T + \mathbf{G}_s \mathbf{G}_c^T), \end{aligned} \quad (10)$$

where

$$\begin{aligned} \tau_{dd} &= \tau_1 + \tau_2 + \tau_m + 2\delta_c + 2\delta_d/3 + 2\delta_s, \\ \tau_{cc} &= \tau_m + 2\delta_c/3 + 2\delta_s, \\ \tau_{ss} &= \tau_m + 2\delta_s/3, \\ \tau_{dc} &= \tau_m + \delta_c + 2\delta_s, \\ \tau_{ds} &= \tau_m + \delta_s, \\ \tau_{cs} &= \tau_m + \delta_s. \end{aligned} \quad (11)$$

The expression in Eq. 10 is the sum of pairwise interactions between the diffusion, crusher and slice-select pulses, similar to the b -matrix for PGSE in [13].

In the absence of any diffusion weighting, the STEAM signal in terms of a steady-state magnetization M_0 and relaxation constants T_1 and T_2 is

$$S_0(\tau_e, \tau_r, \tau_m) = M_0(1 - \exp(-(\tau_r - \tau_m)/T_1)) \exp(-\tau_m/T_1) \exp(-\tau_e/T_2), \quad (12)$$

where τ_e is the echo time and τ_r is the repetition time. Thus, in general we require knowledge of, or must estimate, T_1 and T_2 to estimate diffusion parameters. Normally, $\tau_r \gg \tau_m$ and $\tau_r \gg T_1$, so that $\exp(-(\tau_r - \tau_m)/T_1) \approx 0$ and substituting Eq. 12 into Eq. 8 and taking logs gives

$$\log S = \log M_0 - \tau_m/T_1 - \tau_e/T_2 - B \cdot D. \quad (13)$$

Thus, we can obtain linear estimates of $\log M_0$, T_1 , T_2 and D simultaneously given a set of measurements with sufficiently diverse B , τ_m and τ_e . Specifically, $A = X^*L$, where

$$A^T = (\log M_0, 1/T_1, 1/T_2, D_{xx}, D_{xy}, D_{xz}, D_{yy}, D_{yz}, D_{zz}) \quad (14)$$

contains all the parameters to estimate, $L^T = (\log S_1, \log S_2, \dots, \log S_N)$ contains all the log signals, and X^* is the pseudoinverse of the design matrix X , which has rows

$$(1, -\tau_m, -\tau_e, -B_{xx}, -B_{xy}, -B_{xz}, -B_{yy}, -B_{yz}, -B_{zz}). \quad (15)$$

Single-shell HARDI protocols can keep τ_e , τ_r , and τ_m constant to avoid having to estimate T_1 or T_2 . For multiple b -values often we can keep τ_e constant, but τ_m needs to vary to retain the short- τ_e benefits of STEAM. Thus we can ignore T_2 , but need to estimate T_1 . For fixed τ_m or τ_e , we remove the second or third, respectively, element of A and column of X .

A.2 Compensation

The simple correction for \mathbf{G}_d in Eq. 7 to compensate for the butterfly gradients sets $\mathbf{G}_d - \mathbf{G}$ to the linear combination $g\mathbf{G}_c + h\mathbf{G}_s$ that minimises diffusion weighting in the nominal $b = 0$ images, i.e. when the intended $\mathbf{G} = \mathbf{0}$. Eq. 7 comes from setting $\mathbf{G}_d = g\mathbf{G}_c + h\mathbf{G}_s$ and minimising the trace of the b -matrix in Eq. 10 with respect to g and h to obtain $g = -\delta_c\tau_{dc}(\delta_d\tau_{dd})^{-1}$ and $h = -\delta_s\tau_{ds}(\delta_d\tau_{dd})^{-1}$. The approximation A2 in Eq. 1 simply inverts the compensation to obtain \mathbf{G}_d' .

Another choice of \mathbf{G}_d' for A2 is $(b_1/(\delta_d^2\tau_{dd}))^{\frac{1}{2}}\mathbf{v}_1$, where \mathbf{v}_1 is the primary eigenvector of the b -matrix and b_1 is the corresponding eigenvalue. However, the two choices for \mathbf{G}_d' are very similar in practice and the former is simpler to compute. The maximum difference between the two \mathbf{G}_d' is around 1% over the whole ActiveAxSTEAM protocol.

In practice, \mathbf{G}_s must be in the slice direction, but \mathbf{G}_c can have any orientation. Both choices of \mathbf{G}_d' accommodate arbitrary and separate orientations of \mathbf{G}_c and \mathbf{G}_s .

A.3 Restricted diffusion

For the full sequence outlined in section 2.1,

$$I_k = s_{ddk}G_d^2 + s_{cck}G_c^2 + s_{ssk}G_s^2 + s_{dck}G_dG_c + s_{dsk}G_dG_s + s_{csk}G_cG_s \quad (16)$$

where G_d , G_c and G_s are the components of \mathbf{G}_d , \mathbf{G}_c and \mathbf{G}_s , respectively, in the restricted direction, and

$$s_{ddk} = -2 + 2Y_k(-\delta_d) - Y_k(-(\tau_1 + \tau_2 + 2\delta_c + 2\delta_s + \tau_m)) \quad (17)$$

$$+ 2Y_k(-(\tau_1 + \tau_2 + 2\delta_c + 2\delta_s + \delta_d + \tau_m)) -$$

$$Y_k(-(\tau_1 + \tau_2 + 2\delta_c + 2\delta_s + 2\delta_d + \tau_m)) + 2\lambda_k^2 D\delta_d,$$

$$s_{dck} = (Y_k(\tau_1) + Y_k(\tau_2))(Y_k(\delta_c) - 1)(Y_k(\delta_d) - 1) \times \quad (18)$$

$$(Y_k(\delta_c + 2\delta_s + \tau_m) - 1)Y_k(-(\tau_1 + \tau_2 + 2\delta_c + 2\delta_s + \delta_d + \tau_m)),$$

$$s_{dsk} = (Y_k(\tau_1) + Y_k(\tau_2))(Y_k(\delta_s) - 1)(Y_k(\delta_d) - 1)(Y_k(\delta_s + \tau_m) - 1) \times \quad (19)$$

$$Y_k(-(\tau_1 + \tau_2 + \delta_c + 2\delta_s + \delta_d + \tau_m)),$$

$$s_{cck} = -2 + 2Y_k(-\delta_c) - Y_k(-(2\delta_s + \tau_m)) + 2Y_k(-(\delta_c + 2\delta_s + \tau_m)) \quad (20)$$

$$- Y_k(-(2\delta_c + 2\delta_s) + \tau_m) + 2\lambda_k^2 D\delta_c,$$

$$s_{csk} = 2(Y_k(\delta_c) - 1)(Y_k(\delta_s) - 1)(Y_k(\delta_s + \tau_m) - 1) \times \quad (21)$$

$$Y_k(-(\delta_c + 2\delta_s + \tau_m)),$$

$$s_{ssk} = -2 + 2Y_k(-\delta_s) - Y_k(-\tau_m) + 2Y_k(-(\delta_s + \tau_m)) \quad (22)$$

$$- Y_k(-(2\delta_s + \tau_m)) + 2\lambda_k^2 D\delta_s.$$

To evaluate these expressions, expand them before implementing to avoid numerical problems; code is available from the authors on request.

References

- [1] J. E. Tanner. Use of the stimulated echo in NMR diffusion measurements. *Journal of Chemical Physics*, 52:2523–2526, 1970.
- [2] K. D. Merboldt, W. Hanicke, and J. Frahm. Diffusion imaging using stimulated echoes. *Magnetic Resonance in Medicine*, 19:233–239, 1991.

- [3] O. Brihuega-Moreno, F. P. Heese, and L. D. Hall. Optimization of diffusion measurements using cramer-rao lower bound theory and its application to articular cartilage. *Magnetic Resonance in Medicine*, 50:1069–1076, 2003.
- [4] B. Dhital and R. Turner. Diffusion weighted imaging at 7T with STEAM-EPI and GRAPPA. In *Proc. ISMRM*, page 3994, Stockholm, 2010. ISMRM.
- [5] G. J. Stanisz, A. Szafer, G. A. Wright, and M. Henkelman. An analytical model of restricted diffusion in bovine optic nerve. *Magnetic Resonance in Medicine*, 37:103–111, 1997.
- [6] Y. Assaf, T. Blumenfeld-Katzir, Y. Yovel, and P. J. Basser. AxCaliber: a method for measuring axon diameter distribution from diffusion MRI. *Magnetic Resonance in Medicine*, 59:1347–1354, 2008.
- [7] H. H. Ong and F. W. Wehrli. Quantifying axon diameter and intracellular volume fraction in excised mouse spinal cord with q-space imaging. *NeuroImage*, 51:1360–1366, 2010.
- [8] T. B. Dyrby, W. F. C. Baaré, D. C. Alexander, J. Jelsing, E. Garde, and L. V. Sogaard. An ex-vivo imaging pipeline for producing high quality and high resolution diffusion weighted imaging datasets. *Human Brain Mapping*, 32:544–563, 2011.
- [9] T. M. Shepherd, P. E. Thelwall, G. J. Stanisz, and S. J. Blackband. Aldehyde fixative solutions alter the water relaxation and diffusion properties of nervous tissue. *Magnetic Resonance in Medicine*, 62:26–34, 2009.
- [10] V. J. Wedeen, R. P. Wang, J. D. Schmahmann, T. Benner, W. Y. I. Tseng, G. Dai, D. N. Pandya, P. Hagmann, H. D’Arceuil, and A. J.

- de Crespigny. Diffusion spectrum magnetic resonance imaging (DSI) tractography of crossing fibers. *NeuroImage*, 41:1267–1277, 2008.
- [11] D. C. Alexander, P. L. Hubbard, M. G. Hall, E. A. Moore, M. Ptito, G. J. M. Parker, and T. B. Dyrby. Orientationally invariant indices of axon diameter and density from diffusion MRI. *NeuroImage*, 52:1374–1389, 2010.
- [12] T. B. Dyrby, L. V. Sogaard, M. G. Hall, M. Ptito, and D. C. Alexander. Contrast and stability of the axon diameter index from microstructure imaging with diffusion MRI. *Magnetic Resonance in Medicine*, In press, 2012.
- [13] J. Mattiello, P. J. Basser, and D. Le Bihan. The b matrix in diffusion tensor echo-planar imaging. *Magnetic Resonance in Medicine*, 37:292–300, 1997.
- [14] J. S. Murday and R. M. Cotts. Self-diffusion coefficient of liquid lithium. *Journal of Chemical Physics*, 48:4938–4945, 1968.
- [15] P. Van Gelderen, D. DesPres, P. C. M. van Zijl, and C. T. W. Moonen. Evaluation of restricted diffusion in cylinders. Phosphocreatine in rabbit leg muscle. *Journal of Magnetic Resonance Series B*, 103:255–260, 1994.
- [16] J. Stepisnik. Time-dependent self-diffusion by NMR spin echo. *Physica B*, 183:343–350, 1993.
- [17] D. C. Alexander. A general framework for experiment design in diffusion MRI and its application in measuring direct tissue-microstructure features. *Magnetic Resonance in Medicine*, 60:439–448, 2008.

- [18] D. K. Jones and P. J. Basser. Squashing peanuts and smashing pumpkins: How noise distorts diffusion-weighted MR data. *Magnetic Resonance in Medicine*, 52:979–993, 2004.
- [19] D. C. Alexander and G. J. Barker. Optimal imaging parameters for fibre-orientation estimation in diffusion MRI. *NeuroImage*, 27:357–367, 2005.
- [20] A. Leemans and D. K. Jones. The b-matrix must be rotated when motion correcting diffusion tensor imaging data. *Magnetic Resonance in Medicine*, 61:1336–1349, 2009.
- [21] S. Pajevic and C. Pierpaoli. Color schemes to represent the orientation of anisotropic tissues from diffusion tensor data: application to white matter fiber tract mapping in the human brain. *Magnetic Resonance in Medicine*, 42:526–540, 1999.
- [22] C.-F. Westin, S. E. Maier, B. Khidhir, P. Everett, F. A. Jolesz, and R. Kikinis. Image processing for diffusion tensor magnetic resonance imaging. In *Proc. MICCAI*, pages 441–452, Cambridge, 1999. Springer.
- [23] M. G. Hall and D. C. Alexander. Convergence and parameter choice for Monte-Carlo simulations of diffusion MRI. *IEEE Trans. Medical Imaging*, 28:1354–1364, 2009.
- [24] P. A. Cook, Y. Bai, S. Nedjati-Gilani, K. K. Seunarine, M. G. Hall, G. J. M. Parker, and D. C. Alexander. Camino: Open-source diffusion-MRI reconstruction and processing. In *Proc. 14th Annual Meeting of the ISMRM*, Berlin, 2006.

- [25] A.-S. Lamantia and P. Rakic. Cytological and quantitative characteristics of four cerebral commissures in the rhesus monkey. *The Journal of Comparative Neurology*, 291:520–537, 1990.
- [26] B. Balinov, B. Jonsson, P. Linse, and O. Soderman. The NMR self-diffusion method applied to restricted diffusion. Simulation of echo attenuation from molecules in spheres and between planes. *Journal of Magnetic Resonance. Series A.*, 104:17–25, 1993.
- [27] A. Ianus, B. Siow, H. Zhang, and D. C. Alexander. Gaussian phase distribution approximation of the square wave oscillating gradient spin-echo (SWOGSE) diffusion signal. In *Proc. ISMRM*, page 3561, Melbourne, 2012. ISMRM.
- [28] P. T. Callaghan, A. Coy, D. MacGowan, K. J. Packer, and F. O. Zelaya. Diffraction-like effects in NMR diffusion studies of fluids in porous solids. *Nature*, 351:467–469, 1991.
- [29] P. T. Callaghan. A simple matrix formalism for spin echo analysis of restricted diffusion under generalized gradient waveforms. *Journal of Magnetic Resonance*, 129:74–84, 1997.
- [30] D. Grebenkov. NMR survey of reflected brownian motion. *Reviews of Modern Physics*, 79:1077–1137, 2007.
- [31] I. Drobnjak, H. Zhang, M. G. Hall, and D. C. Alexander. The matrix formalism for generalised gradients with time-varying orientation in diffusion NMR. *Journal of Magnetic Resonance*, 210:151–157, 2011.
- [32] R. M. Cotts, M. J. R. Hoch, T. Sun, and T. Marker. Pulsed field gradient stimulated echo methods for improved NMR diffusion measurements of

- heterogeneous systems. *Journal of Magnetic Resonance*, 83:252–266, 1989.
- [33] J. Finsterbusch. Cross-term-compensated pulse-gradient stimulated echo MR with asymmetric gradient pulse lengths. *Journal of Magnetic Resonance*, 193:41–48, 2008.
- [34] W. S. Price. Pulsed-field gradient nuclear magnetic resonance as a tool for studying translational diffusion: Part 1. basic theory. *Concepts in Magnetic Resonance*, 9:299–336, 1997.

N	K	$ \mathbf{G}_d /\text{mT m}^{-1}$	Δ/ms	δ_d/ms	$b/\text{s mm}^{-2}$	τ_e/ms	τ_r/ms
103	25	300.0	12.9	5.6	2243	36.8	2600
106	25	219.2	20.4	7.0	3084	36.8	2600
80	25	300.0	18.8	10.5	10838	36.8	2600

(a)

N	K	$ \mathbf{G}_d /\text{mT m}^{-1}$	τ_m/ms	δ_d/ms	τ_1/ms	$b/\text{s mm}^{-2}$	τ_e/ms	τ_r/ms
103	25	300.0	6.0	5.0	0.0	2306	26.0	2600
108	25	113.5	137.0	5.0	3.4	3425	26.0	2600
78	25	260.4	137.0	4.5	3.9	14631	26.0	2600

(b)

Table 1: The (a) ActiveAxPGSE and (b) ActiveAxSTEAM protocols. Both come from the experiment design optimisation in [17, 12] with $G_{\max} = 300\text{mT m}^{-1}$. N is the number of diffusion weighted images in each shell. K is the number of nominal $b = 0$ images associated with each shell. The total number of images in each protocol is thus 364. The nominal $b = 0$ images associated with each shell in ActiveAxSTEAM have the same τ_m as the diffusion weighted images in that shell. The compensated STEAM protocol ActiveAxSTEAMCOMP follows (b), but replaces each \mathbf{G}_d according to Eq. 7.

	Uncompensated						Compensated			
	A1		A2		A3		A1/A2		A3	
	\perp	\parallel	\perp	\parallel	\perp	\parallel	\perp	\parallel	\perp	\parallel
FA	0.513	0.884	0.572	0.495	0.572	0.495	0.576	0.574	0.576	0.574
std	0.035	0.171	0.026	0.043	0.026	0.043	0.020	0.021	0.020	0.021
λ_1	5.508	1.524	5.270	3.378	5.270	3.378	5.568	5.544	5.568	5.544
std	0.260	0.272	0.209	0.187	0.209	0.187	0.161	0.166	0.161	0.166
α	4.603	63.752	2.505	5.085	2.505	5.085	1.921	1.999	1.921	1.999
γ	5.351	1.890	6.264	5.345	6.264	5.345	6.791	6.712	6.791	6.712

Table 2: Statistics from simulations with anisotropic DTs for each approximation using the $b = 3425 \text{ s mm}^{-2}$ shell of ActiveAxSTEAM, and SNR of 20. The units of λ_1 are $10^{-10} \text{ m}^2 \text{ s}^{-1}$; the units of α are degrees. The true FA is 0.603 and the true λ_1 is $6 \times 10^{-10} \text{ m}^2 \text{ s}^{-1}$. Higher γ is better in this experiment.

	Uncompensated			Compensated	
	A1	A2	A3	A1/A2	A3
FA	0.284	0.175	0.175	0.058	0.058
std	0.075	0.033	0.033	0.019	0.019
λ_1	3.809	3.660	3.660	4.021	4.021
std	0.297	0.168	0.168	0.102	0.102
γ	1.516	0.848	0.848	0.412	0.412

Table 3: Statistics, as in table 2, from simulations with isotropic DTs. The true FA is 0; the true λ_1 is $4 \times 10^{-10} \text{ m}^2 \text{ s}^{-1}$. Here γ should be zero.

	Uncompensated						Compensated			
	A1		A2		A3		A1/A2		A3	
	\perp	\parallel	\perp	\parallel	\perp	\parallel	\perp	\parallel	\perp	\parallel
FA	0.873	0.862	0.862	0.863	0.862	0.863	0.864	0.864	0.864	0.864
std	0.018	0.017	0.018	0.017	0.018	0.017	0.017	0.017	0.017	0.017
λ_1	15.980	17.508	16.197	16.290	16.197	16.290	16.341	16.344	16.341	16.344
std	0.564	0.573	0.573	0.529	0.573	0.529	0.526	0.528	0.526	0.528
α	12.474	2.555	1.450	1.463	1.450	1.463	1.432	1.433	1.432	1.433
γ	7.249	7.422	7.359	7.340	7.359	7.340	7.378	7.378	7.378	7.378

Table 4: Simulation statistics for anisotropic diffusion with the human protocol. The true FA is 0.87 and the true λ_1 is $1.7 \times 10^{-9} \text{ m}^2\text{s}^{-1}$.

	Uncompensated			Compensated	
	A1	A2	A3	A1/A2	A3
FA	0.240	0.099	0.099	0.099	0.099
std	0.044	0.032	0.032	0.032	0.032
λ_1	5.139	4.324	4.324	4.326	4.326
std	0.313	0.252	0.252	0.251	0.251
γ	3.149	0.444	0.444	0.416	0.416

Table 5: Simulation statistics for isotropic diffusion with the human protocol. The true FA is 0 and the true E_1 is $0.7 \times 10^{-9} \text{ m}^2\text{s}^{-1}$.

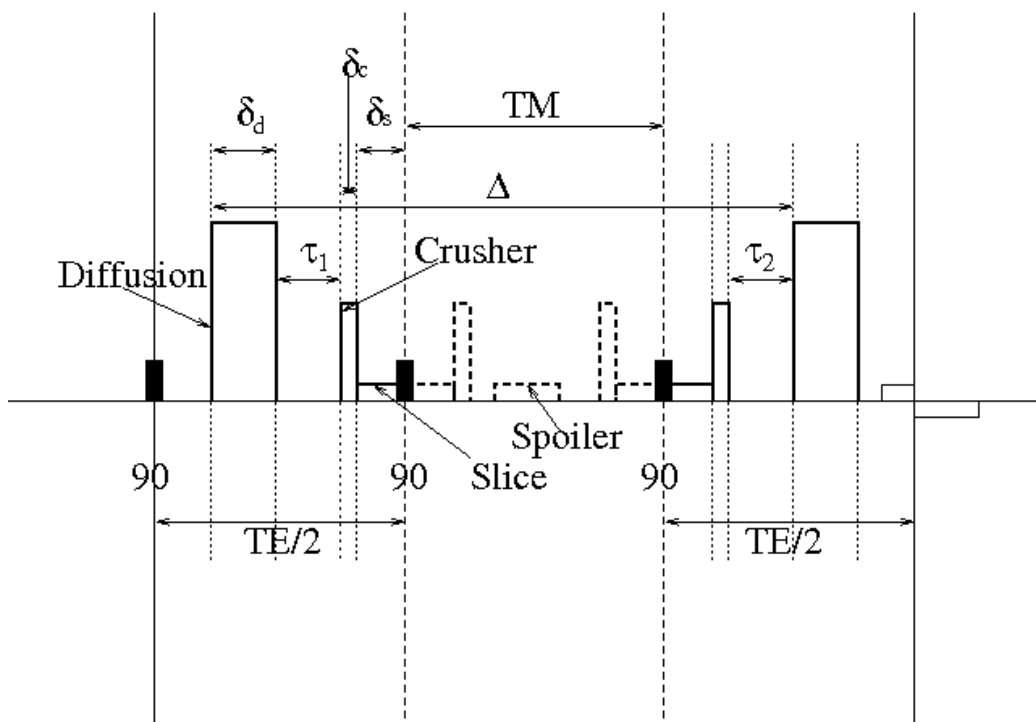


Figure 1: Diagram of the STEAM pulse sequence.

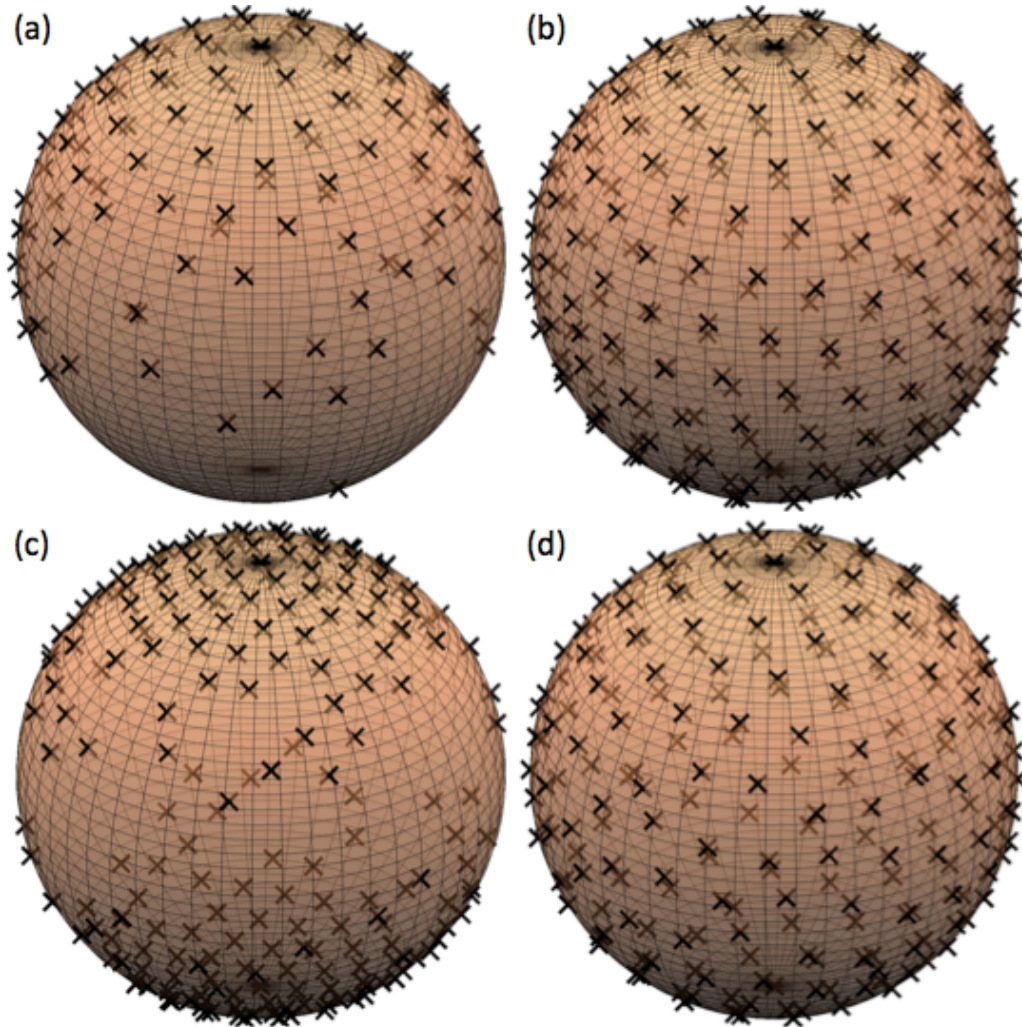


Figure 2: Illustration of the target and effective gradient directions in the STEAM protocols using the 108 directions in the $b = 3425 \text{ s mm}^{-2}$ shell of the ActiveAxSTEAM protocol. A black cross marks each direction; shaded crosses are on the far side of the sphere. Panel (a) is the target set of gradient directions. Panel (b) shows the target set with a cross in both the positive and negative gradient direction to show the isotropic distribution more clearly. Panel (c) shows the set of effective gradient directions, i.e. the direction of \mathbf{G}_d' in Eq. 1, without compensation (ActiveAxSTEAM); they skew strongly towards the slice direction. Panel (d) shows the effective gradient directions after compensation (ActiveAxSTEAMCOMP), which are close to the target set.

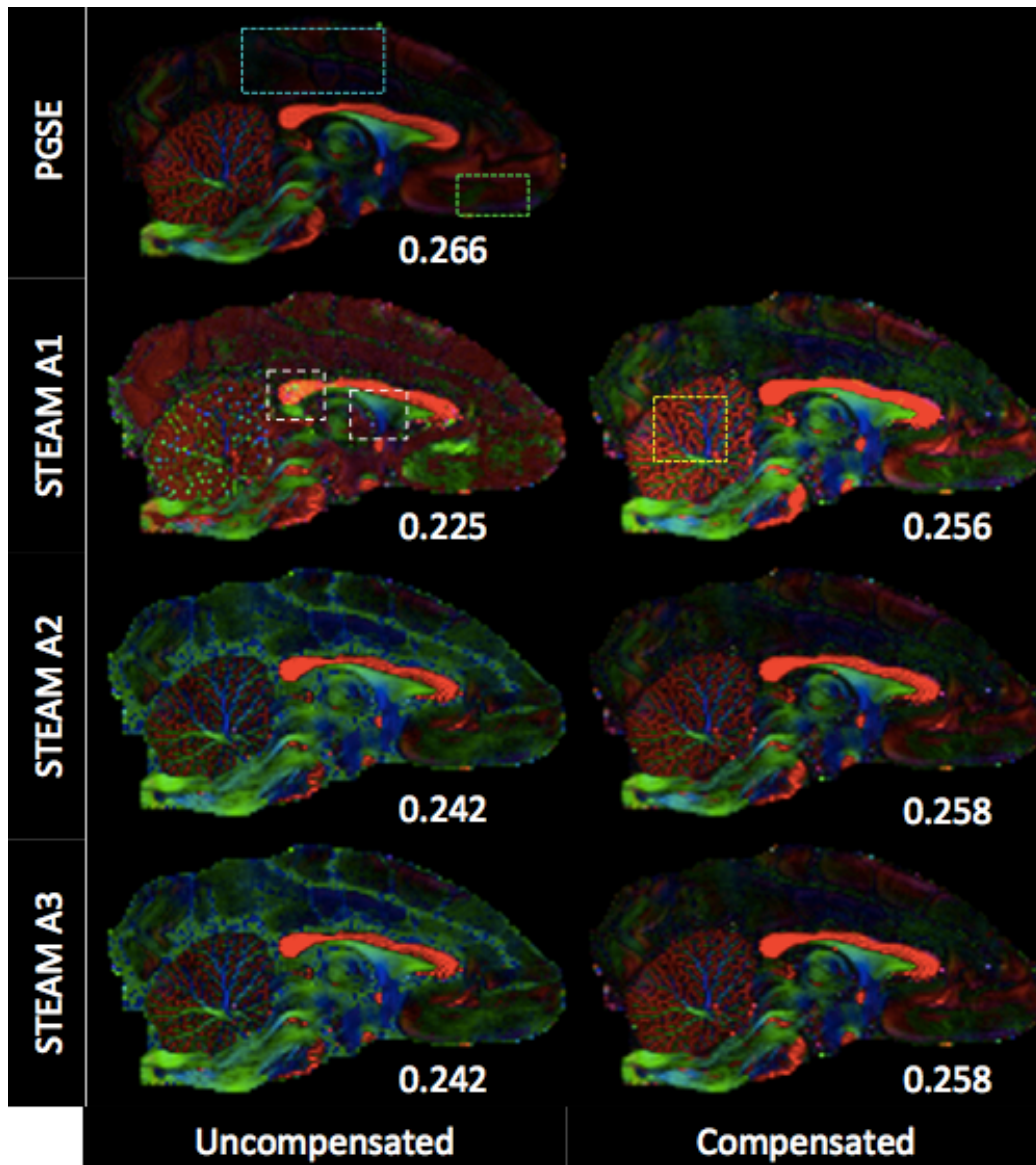


Figure 3: Direction-encoded colour maps [21] for the mid-sagittal slice of the monkey brain from the $b = 3084 \text{ s mm}^{-2}$ shell of ActiveAxPGSE (top left), the $b = 3425 \text{ s mm}^{-2}$ shell of ActiveAxSTEAM (left) and ActiveAxSTEAM-COMP (right). Rows 2-4 show the maps reconstructed with A1, A2 and A3, respectively. The numbers quantify the orientational similarity (definition in the text) between each STEAM map and the PGSE map. The number in the PGSE panel is the similarity of the maps from the $b = 3084 \text{ s mm}^{-2}$ and $b = 2243 \text{ s mm}^{-2}$ shells of ActiveAxPGSE.

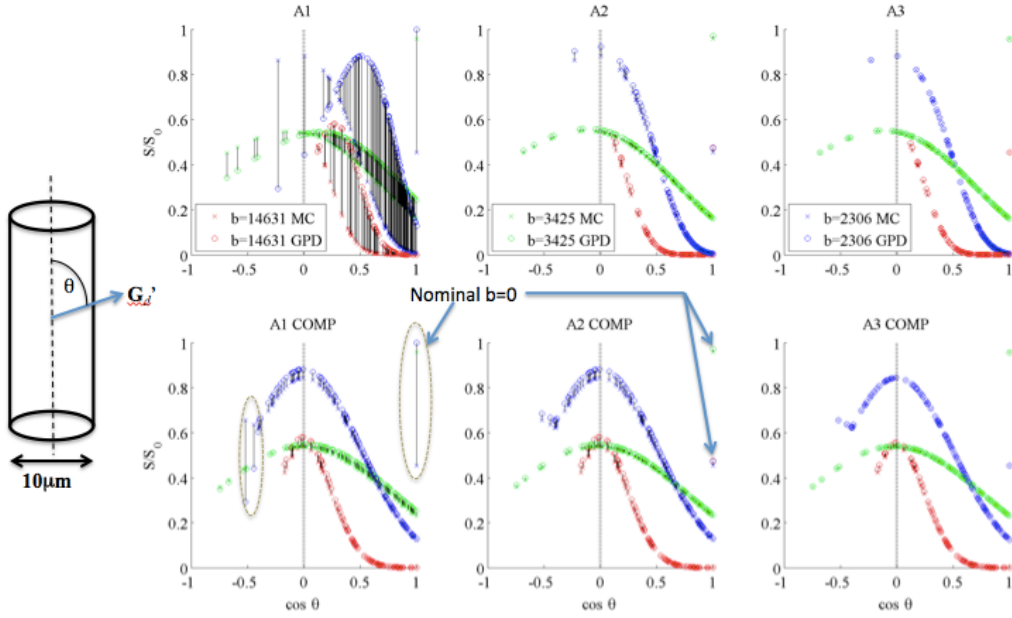


Figure 4: Comparison of the STEAM signal estimates using A1, A2 and A3 from particles restricted within an impermeable cylinder of diameter $10\mu\text{m}$ with ground-truth signals from MC simulation. Each panel plots normalized signals, S/S_0 , against $\cos \theta$ where θ is the angle between the effective gradient direction \mathbf{G}_d' (Eq. 1) and the cylinder axis (positive slice direction). A black line connects each estimate with the corresponding ground truth. The top row shows plots for the ActiveAxSTEAM protocol. The bottom row shows equivalent plots for ActiveAxSTEAMCOMP. The dotted vertical line indicates the perpendicular gradient orientation where we expect the largest signal. The ellipses in the bottom left figure highlight the imperfectly compensated measurements.

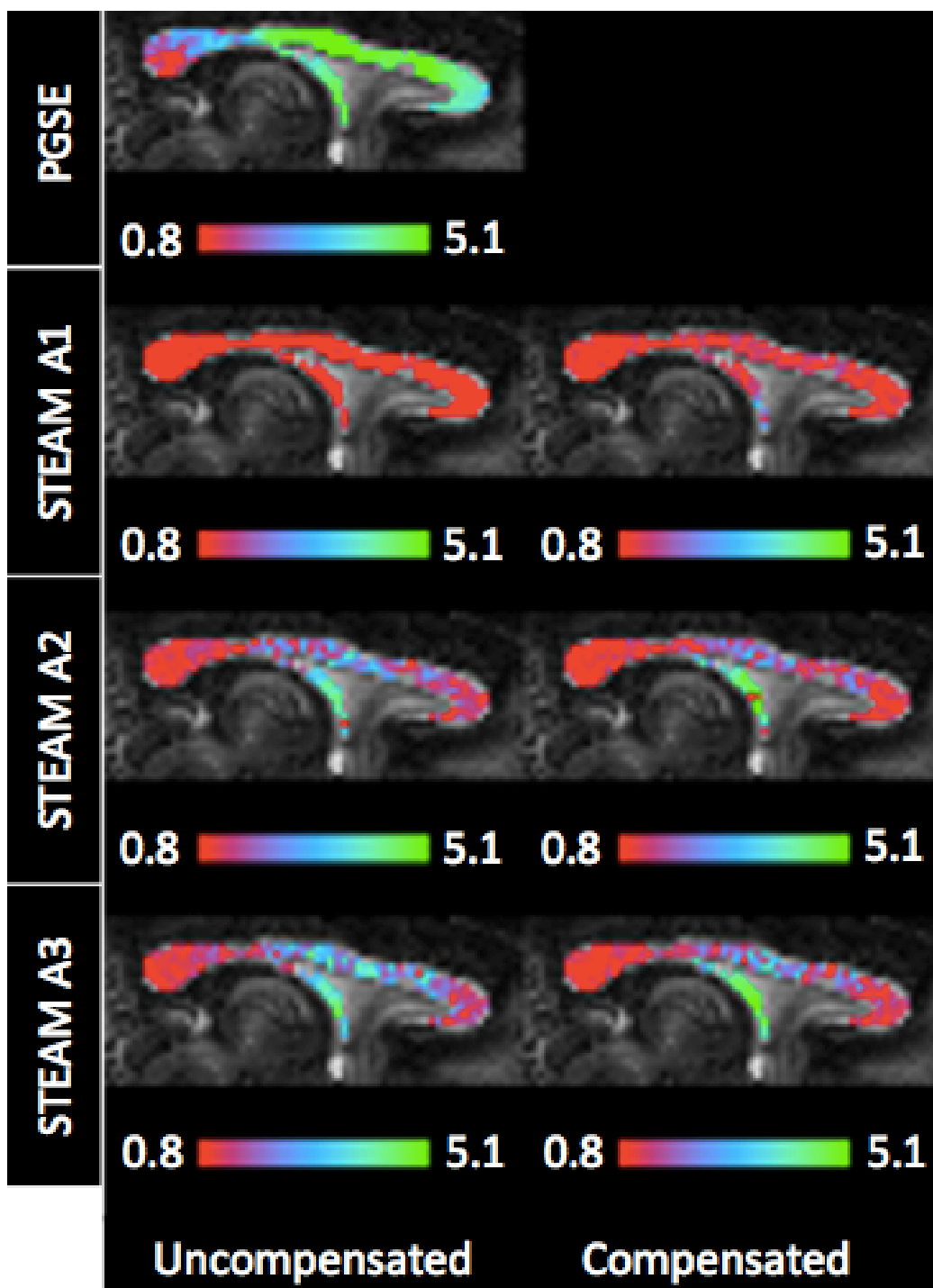


Figure 5: Maps of the axon diameter index [11] over the mid-sagittal corpus callosum recovered from the ActiveAxPGSE data (top left), ActiveAxSTEAM (left) and ActiveAxSTEAMCOMP (right) with each approximation.